Water in carbon nanotubes: Adsorption isotherms and thermodynamic properties from molecular simulation

A. Striolo[a)]
Department of Chemical Engineering, Vanderbilt University, Nashville, Tennessee 37235-1604

A. A. Chialvo
Chemical Sciences Division, Oak Ridge National Laboratory, Oak Ridge, Tennessee 37831-6110

K. E. Gubbins
Department of Chemical Engineering, North Carolina State University, 113 Riddick Labs, Raleigh, North Carolina 27695-7905

P. T. Cummings
Department of Chemical Engineering, Vanderbilt University, Nashville, Tennessee 37235-1604 and Chemical Sciences Division, Oak Ridge National Laboratory, Oak Ridge, Tennessee 37831-6110

Grand canonical Monte Carlo simulations are performed to study the adsorption of water in single-walled (6:6), (8:8), (10:10), (12:12), and (20:20) carbon nanotubes in the 248–548 K temperature range. At room temperature the resulting adsorption isotherms in (10:10) and wider single-walled carbon nanotubes (SWCNs) are characterized by negligible water uptake at low pressures, sudden and complete pore filling once a threshold pressure is reached, and wide adsorption/desorption hysteresis loops. The width of the hysteresis loops decreases as pore diameter narrows and it becomes negligible for water adsorption in (8:8) and (6:6) SWCNs. Results for the isosteric heat of adsorption, density profiles along the pore axis and across the pore radii, order parameter across the pore radii, and x-ray diffraction patterns are presented. Layered structures are observed when the internal diameter of the nanotubes is commensurate to the establishment of a hydrogen-bonded network. The structure of water in (8:8) and (10:10) SWCNs is ordered when the temperature is 298 and 248 K, respectively. By simulating adsorption isotherms at various temperatures, the hysteresis critical temperature, e.g., the lowest temperature at which no hysteresis can be detected, is determined for water adsorbed in (20:20), (12:12), and (10:10) SWCNs. The hysteresis critical temperature is lower than the vapor-liquid critical temperature for bulk Simple Point Charge-Extended (SPC/E) water model. © *2005 American Institute of Physics.*
[DOI: 10.1063/1.1924697]

I. INTRODUCTION

Carbon nanotubes were first observed by Iijima[1] and several methods are currently available for their production.[2,3] Among them, the catalytic-arc method[4,5] yields single-walled carbon nanotubes (SWCNs) with a narrow pore-size distribution. Early theoretical studies predicted that SWCNs behave as either metals or semiconductors depending on the arrangement of carbon atoms;[6–8] could be used as storage devices for hydrogen;[9] may enhance chemical reactions which involve a separation of charges.[10] Other studies indicated that the electronic properties of SWCNs are sensitive to the adsorption of $NO_2, O_2,$ and NH_3 (Refs. 11–13), and that they could be used to produce one-dimensional nanowires,[14,15] to build assemblies for controlled transport of water for nanofluidic devices,[16] and to stabilize novel crystal structures of ionic systems at temperatures at which the bulk material would be fluid.[17] However, the presence of water vapor could compromise the performance of the nanotubes.

Thus, it is crucial to understand and predict the thermodynamic behavior of water confined within SWCNs. Furthermore, the understanding of adsorption isotherms and density distributions for confined fluids is of significant relevance for the understanding of phase behavior of confined fluids[18] and biological systems such as ion channels or cellular membranes.[19–22]

Water adsorption in carbon matrices is known to be strongly affected by the presence and density of oxygenated groups on the carbon surfaces.[23–28] In the absence of such groups, the adsorption of water is insignificant at pressures below the capillary-condensation pressure and it is usually accompanied by large adsorption-desorption hysteresis loops.[29,30] This behavior results from the strong water-water associative interactions, relative to the weak carbon-water dispersive interactions.[31] As the surface density of oxygenated groups increases, water adsorption occurs at increasingly lower pressures, and as the pressure increases a continuous pore filling may occur. Müller *et al.*[24] and Jorge *et al.*[32] showed that, while the chemical nature of the oxygenated groups does not have a significant effect on the adsorption isotherms for water, their location within carbon-slit

---
a)Author to whom correspondence should be addressed. Electronic mail: alberto.striolo@Vanderbilt.Edu

pores can significantly alter the simulated adsorption isotherms and the calculated Henry constants. Because of the small sizes that characterize carbon matrices, their peculiar morphologies, and the frequent appearance of long-lived metastable states for the adsorbed water, experimental observations can benefit by coupling to molecular simulations as a powerful tool for the investigation of adsorption phenomena.

The interest in understanding the effect of confinement on the properties of water has grown significantly in recent years, as manifested by the number of publications that we now summarize. Among available experimental results for water in carbons, Bekyarova et al.[33] reported experimental adsorption isotherms in carbon nanohorns. Their results indicate that water can be adsorbed within hydrophobic nanotubes at pressures below saturation, and that large adsorption-desorption hysteresis loops can be observed. Maniwa et al.[34] reported x-ray diffraction experiments for water adsorbed in (10:10) SWCNs in the 90–570 K temperature range. They observed that water can be adsorbed within these nanotubes at pressures below saturation, that the adsorption-desorption hysteresis loops are not detectable at temperatures above 450 K, and that confined water undergoes a structural transition to an ordered phase at temperatures below 235 K. This ordered structure does not correspond to the hexagonal ice typical for bulk water at atmospheric pressure, but it resembles the heptagonal and octagonal ice structures theoretically predicted by Koga et al.[35] In contrast to the atmospheric-pressure experiments of Maniwa et al.,[34] Koga et al.[35] obtained ordered structures for confined water only when an axial pressure of 50–500 MPa was applied.

Among relevant theoretical contributions, Martí and Gordillo[36] calculated the vibrational and rotational spectra of confined liquid water at 298 K and found that significant shifts in the positions of the spectral bands are directly related to the tube radii. They also observed that confinement of supercritical water induces faster changes in the oxygen velocities compared to values for the bulk, although water diffusion is slower.[37] Brovchenko et al.[38] found that when water is confined in a hydrophobic cylindrical pore, the diffusion along the pore axis is faster than the bulk self-diffusion. Noon et al.[39] studied systems composed of short nanotubes (2 nm in length) in water at 300 K, and found that (5:5) SWCNs are too narrow to accommodate water molecules in their interior. These authors found that water could exist within wider SWCNs and that the confined water may form hydrogen-bonded "*solidlike wrapped-around ice sheets.*" As mentioned above, Koga et al. studied the properties of water confined in carbon nanotubes with diameters ranging from 1.1 to 1.4 nm and found an evidence of a first-order freezing transition to the hexagonal and heptagonal ice nanotubes, and a continuous phase transformation into solidlike square or pentagonal ice nanotubes.[35] Brovchenko et al.[40] studied the vapor-liquid phase envelope for water confined in cylindrical pores of radius 1.2 nm and observed that the vapor-liquid critical temperature for confined water can be 200 K lower than that of bulk water. Rivera et al.[41] studied the phase equilibria of confined water-CO_2 systems by quench molecular dynamics, and observed a

pronounced layering in the liquid aqueous phase as the CO_2 pressure increases. When a cylindrical nanopore is in contact with bulk water, Giaya and Thompson[42] indicated that the density of confined water can be larger than that of bulk water when the bulk is vapor, but more interestingly that when the bulk is liquid it is possible that the density of confined water is vaporlike.

Recently, our group studied water adsorption in carbon-slit pores and in SWCNs at 298 K by grand canonical Monte Carlo simulations.[43,44] In agreement with others,[24,28,29,45] our results indicated that the room temperature adsorption isotherms are of type V in the International Union of Pure and Applied Chemists (IUPAC) classification.[23,31] Pore-sieving effects were observed in carbon-slit pores narrower than 0.7 nm.[43] Adsorption isotherms simulated in SWCNs exhibited pore filling at lower pressures and narrower adsorption-desorption hysteresis loops compared to those simulated in carbon-slit pores of similar widths.[44] In both carbon-slit pores and SWCNs water adsorption occurs via the formation and growth of clusters of hydrogen-bonded water molecules, while desorption takes place after the appearance of bubbles that disrupt the hydrogen-bonded network of adsorbed water molecules. The appearance of adsorption-desorption hysteresis loops may be a consequence of the different mechanisms followed by the system during adsorption or desorption. Here we report results for the adsorption of water in SWCNs of several diameters in the temperature range 248–548 K. Chemical heterogeneity in the porous material and pore interconnectivity are not considered, but they will be the subject of our future work.[46,47] By ignoring pore imperfections it is possible to modulate the pore-water interactions by adjusting the pore size. Pore-water interactions are more attractive in narrower pores, but water molecules adsorbed in narrow pores are confined in regions of limited dimensions (one-dimensional regions for narrow SWCNs). Under these circumstances, the tetrahedral hydrogen-bonded structure characteristic of liquid water is distorted, as previously observed for supercritical water confined in SWCNs,[48] and for water confined in narrow carbon-slit pores,[43] thus resulting in less favorable water-water interactions.

The goal of the present work is to understand the effect of nanotube diameters on the features of simulated water adsorption isotherms. In addition to adsorption isotherms, we report the results for the limit at low coverage of the isosteric heat of adsorption, which provides macroscopic evidence of pore-water effective interactions. We are interested in characterizing the structure of water confined in SWCNs of different diameters and we discuss the density profiles, order parameters, dipole-dipole correlation functions, x-ray diffraction patterns, as well as representative simulation snapshots. We also seek to understand the effect of temperature on the structure of confined water (possible disorder-to-order phase transitions at low temperatures) and on the features of simulated adsorption isotherms, especially at high temperatures.

The remainder of the manuscript is organized as follows: in Sec. II we present the simulation algorithms employed to
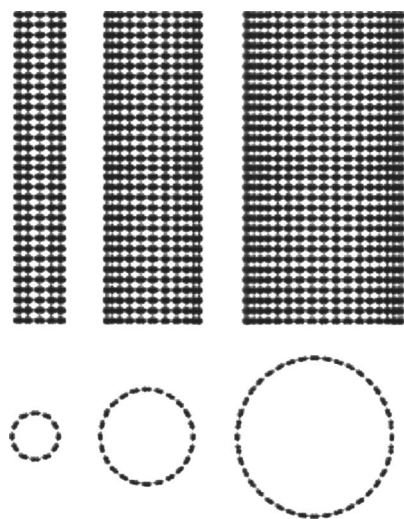
FIG. 1. Schematic view of (6:6) (left), (12:12) (center), and (20:20) (right) single-walled carbon nanotubes (SWCN) considered in this work.

accomplish our goals; in Sec. III we discuss our results; in the last section we provide a brief summary of the material presented.

II. SIMULATION DETAILS

Water adsorption is simulated in (6:6), (8:8), (10:10), (12:12), and (20:20) SWCNs. The diameters of (6:6), (8:8), (10:10), (12:12), and (20:20) SWCNs, based on the distance between carbon-atom centers on opposite sides of the SWCN, are 0.81, 1.08, 1.36, 1.63, and 2.71 nm, respectively [see Fig. 1 for a schematic representation of (6:6), (12:12), and (20:20) SWCNs]. The effective diameters available to adsorbed water molecules are somewhat less than the values just reported. Their lower bound can be estimated from the nominal diameters just reported reduced by the Lennard-Jones diameter of one carbon atom, 0.34 nm. Simulated (6:6) SWCNs are 4.9 nm long, while all the other SWCNs are 3.7 nm long. Periodic boundary conditions are implemented along the pore axis so that the pores are effectively infinitely long. No water is allowed outside the nanotubes, thus the pores should be imagined as surrounded by vacuum.

The Simple Point Charge-Extended (SPC/E) water model[49] was chosen to describe the water molecules, i.e., water is represented as a sphere with the oxygen atom located in its center. The center of the sphere corresponds to the site responsible for dispersive oxygen-oxygen interactions, described by a Lennard-Jones potential. The sites representative of the hydrogen atoms are located at a distance of 0.1 nm from the oxygen site; the hydrogen-oxygen-hydrogen angle is 109.5°. Partial charges are placed on the oxygen and on the hydrogen sites. The charge on the oxygen site equals $-0.8476e$, while each of those located at the hydrogen sites equals $+0.4238e$. The water-water interaction potential is given by

TABLE I. Lennard-Jones parameters for the water-water and carbon-carbon dispersive interactions. ε is the minimum depth of the interaction potential and σ is the center-to-center distance when the potential passes through zero. k is Boltzmann's constant.

	σ (nm)	ε/k (K)
Water-water	0.3166	78.23
Carbon-carbon	0.340	28.00

$$u_{\text{WW}}(r_{12},\omega_1,\omega_2) = \sum_{i=1}^{3} \sum_{j=1}^{3} \frac{q_i q_j}{4\pi\varepsilon_0 r_{ij}} + 4\varepsilon_{\text{WW}}\left[\left(\frac{\sigma_{\text{WW}}}{r_{\text{WW}}}\right)^{12} - \left(\frac{\sigma_{\text{WW}}}{r_{\text{WW}}}\right)^{6}\right]. \quad (1)$$

In Eq. (1), ε_0 is the permittivity of vacuum (8.854×10^{-12} C^2 J^{-1} m^{-1}), q_i is the partial charge localized on each charged site, r_{12} is the distance between the centers of mass of the pair of water molecules, ω_i indicates the molecular orientation, r_{ij} is the distance between sites in different molecules, r_{WW} is the distance between oxygen sites in the pair of water molecules, and ε_{WW} and σ_{WW} are the corresponding Lennard-Jones energy and size interaction parameters (see Table I).

Each carbon atom in the system is represented as a Lennard-Jones sphere whose interaction parameters were taken from Steele.[50] The carbon-water interaction potential u_{WC} is given by

$$u_{\text{WC}}(r_{\text{WC}}) = 4\varepsilon_{\text{WC}}\left[\left(\frac{\sigma_{\text{WC}}}{r_{\text{WC}}}\right)^{12} - \left(\frac{\sigma_{\text{WC}}}{r_{\text{WC}}}\right)^{6}\right]. \quad (2)$$

In Eq. (2) r_{WC} is the distance between the oxygen in the water molecule and the carbon atom. The Lennard-Jones parameters for the unlike interactions, σ_{WC} and ε_{WC}, are obtained from the water-water and carbon-carbon parameters (see Table I) by the Lorentz–Berthelot combining rules:

$$\sigma_{ij} = \frac{\sigma_{ii} + \sigma_{jj}}{2},$$

$$\varepsilon_{ij} = \sqrt{\varepsilon_{ii}\varepsilon_{jj}}. \quad (3)$$

The potential energy of a water molecule within the pore is given by the sum of its interactions with the carbon sites in the pore wall, plus those with other water molecules. The pore-water potential is obtained by explicitly considering each carbon-water pair interaction. Water-water interactions were treated with a spherical cutoff at 1.0 nm. Results for the selected systems were reproduced using the original cutoff for the SPC/E model for water, 0.9 nm,[49] and no appreciable difference was observed. For computational efficiency a grid was built to account for dispersive solid-water interactions with spacing of 0.02 nm, and a linear interpolation was used to compute the values between the points in the grid.

The grand canonical Monte Carlo (GCMC) method[51–53] was used to simulate water adsorption, i.e., volume, temperature, and adsorbate chemical potential were kept constant. The number of adsorbate molecules was allowed to fluctuate, as well as the location and the orientation of each adsorbed

molecule within the pore. Trial moves, randomly chosen with equal probability to ensure microscopic detailed balance, were translation, rotation, insertion, and deletion of water molecules. The maximum translation vector was automatically adjusted to obtain an acceptance ratio of about 0.35. The molecular orientations of water and corresponding rotations were described in terms of quaternions.[52] No limitation was imposed on the maximum rotational angle, resulting in an acceptance ratio of 0.20 for the rotation trial moves.

Equilibration runs as long as 5×10^8 trial moves were required, after which the production phase involved up to 4×10^9 trial moves. The largest systems simulated comprised 1200 carbon atoms and ≈ 500 adsorbed water molecules. The number of accepted insertion/deletion trial moves ensured that each water molecule confined within the nanotubes was substituted at least 10 000 times during a typical simulation run.

For the adsorption path of the isotherms, to mimic experimental procedures, the pores were first considered empty. Simulation runs were performed at increasing chemical potentials, and the resulting configurations at the specified conditions were used to initiate the subsequent calculations at higher chemical potentials. Desorption cycles were initiated with a typical configuration of a filled pore, and subsequently, the chemical potential was reduced until the pores were emptied from previously confined water. The method introduced in Ref. 24 was adopted to obtain the reduced pressure of the bulk phase in equilibrium with the adsorbate at various chemical potentials. This method relies on the calculation of density and chemical potential of the saturated bulk vapor phase at each temperature. We repeated our GCMC simulations in a cubic box of size 3.0 nm in which no carbon atoms are present and in which the periodic image convention is applied in the three directions.[43] We started our simulations from an empty box and we gradually increased the chemical potential until the liquid phase was obtained. We considered as the saturated vapor phase the system with the highest chemical potential at which the density of water was vaporlike. It has been pointed out that, because of the limitations of the GCMC algorithm, our method underpredicts the bulk relative pressures, thus our adsorption isotherms should be shifted somewhat towards larger pressures.[54] Consequently, our method for the prediction of bulk relative pressures is semiquantitative, but it should be noted that if a more quantitative prediction of water adsorption isotherms is required, more sophisticated carbon-water interaction potentials should be used.[55]

Most simulated adsorption isotherms exhibit adsorption-desorption hysteresis loops, in analogy with experimental measurements for water adsorption in carbons.[26,31] Sarkisov and Monson showed that, for Lennard-Jones fluids adsorbed in silica-based materials, the GCMC method yields results that agree with those obtained by the grand canonical molecular dynamics algorithm, which in turn reproduces the mechanism of adsorption and desorption that occurs in experiments. They concluded that the appearance of hysteresis loops in adsorption isotherms for Lennard-Jones fluids in mesopores is a manifestation of long-lived metastable states for the confined system.[56,57] Similar calculations have yet to

be performed for water in carbons. Because of the strongly associating water-water interactions the conclusions reached in the case of Lennard-Jones fluid adsorption may not hold for water adsorption.

The amount of adsorbed water, as a function of pressure, is reported in terms of surface coverage ξ defined as the number of adsorbed water molecules per square nanometer of porous surface. The porous (geometrical) surface area was calculated as $\pi D H$, where D is the SWCN diameter, computed as the distance between opposite carbon atoms across the diameter, and H is the pore length, 3.7 or 4.9 nm in the cases presented here.

The isosteric heat of adsorption was computed according to the expression:[51]

$$q_{st} \cong - \frac{\langle NU \rangle - \langle N \rangle \langle U \rangle}{\langle N^2 \rangle - \langle N \rangle \langle N \rangle} + kT, \tag{4}$$

where N is the total number of adsorbed water molecules, U is the system configurational internal energy, k is the Boltzmann constant, and the angular brackets denote ensemble averages.

The oxygen- and hydrogen-atom axial density profiles were computed as

$$\rho_i^z(z) = \frac{4}{\pi} \frac{\langle N_i^z(z, z+dz) \rangle}{\langle N_i \rangle D^2 dz}. \tag{5}$$

In Eq. (5), subscript i is either for oxygen or hydrogen, D is the SWCN diameter, dz is the width of the pore slab considered along the pore axis to compute the local density, N_i is the number of adsorbed atoms i, and N_i^z is the number of atoms i adsorbed in the slab comprised between the axial coordinates z and $z+dz$.

The radial density profiles were computed as

$$\rho_i^R(R) = \frac{\langle N_i^R(R, R+dR) \rangle}{\langle N_i \rangle d\Gamma}, \tag{6}$$

where R is the radial distance from the pore axis and $d\Gamma$ is the surface of the annulus considered to compute the oxygen- and hydrogen-atom densities.

The order parameters S and T across the pore diameter were computed as

$$S = \frac{3\langle \cos^2 \psi \rangle - 1}{2} \tag{7}$$

and

$$T = \frac{3\langle \cos^2 \zeta \rangle - 1}{2}. \tag{8}$$

In Eqs. (7) and (8) ψ and ζ are the angles between the dipole moment of the water molecule and the direction of the pore axis and of the pore radius, respectively. When the water dipoles are parallel to the pore axis S equals 1; when the dipoles are perpendicular to the pore axis S equals -0.5. When the water dipoles are parallel to the pore radius T equals 1, when they are perpendicular to the pore radius T equals -0.5. Three ordered states are possible for confined water molecules: when the dipole moments are parallel to the pore axis and perpendicular to the pore radius S equals 1 and

T equals -0.5; when the dipoles are perpendicular to the pore axis and to the pore radius S and T both equal -0.5; when the dipoles are perpendicular to the pore axis and parallel to the pore radius S equals -0.5 and T equals 1.

The dipole-dipole correlation function as a function of the center-to-center separation between confined water molecules was computed as

$$\gamma(r) = \langle \cos \delta \rangle, \qquad (9)$$

where δ is the angle formed by the dipole moments of the water molecules separated by the center-to-center separation r. When $\gamma(r)$ equals 1 the dipole moments are parallel, when it equals -1 they are antiparallel. When there is no correlation between the orientation of the dipole moments separated by r, $\gamma(r)=0$.

Following Gnutzmann and Vogel,[58] the structure of confined water was characterized for selected simulation snapshots by the use of the Debye function:[59]

$$I(b) = \sum_n \sum_m f_n(b) f_m(b) [\sin(2\pi b r_{nm})]/(2\pi b r_{nm}). \qquad (10)$$

In Eq. (10) the intensity I of the diffracted coherent radiation is a function of the length of the vector in reciprocal space $[b=2\sin(\theta/\lambda)]$, λ is the wavelength of the incident light, θ is the Bragg angle, r_{nm} is the separation between atoms n and m. The functions $f_n(b)$ and $f_m(b)$ are the atomic scattering amplitudes for the atoms n and m. Debye-functional analyses are routinely used to infer the structure of catalytic nanoparticles from the available experimental x-ray diffraction patterns.[60] Only the positions of confined oxygen atoms were used here to compute the diffraction patterns. Values for the atomic scattering amplitudes for molecular oxygen were obtained from Cromer and Mann.[61] The wavelength of the incident light was considered equal to that of synchrotron radiation (0.10 nm) to compare with the available experimental data.[34]

III. RESULTS AND DISCUSSION

A. Adsorption isotherms at 298 K

In Fig. 2 we report the simulated adsorption isotherms for water in (6:6), (8:8), (10:10), (12:12), and (20:20) SWCNs at 298 K. Adsorption isotherms simulated in (10:10), (12:12), and (20:20) SWCNs are of type V in the IUPAC classification,[23,31] characterized by negligible water uptake at low pressures, sudden and complete pore filling once a threshold pressure is reached, and wide adsorption-desorption hysteresis loops. No hysteresis can be observed for water adsorption in (6:6) and in (8:8) SWCNs at this temperature, and the amount of water adsorbed in (6:6) SWCNs increases gradually as pressure increases. As noted previously,[44] the capillary-condensation pressure and the width of the adsorption-desorption hysteresis loops decrease with decreasing pore diameter for (8:8) and larger SWCNs. A pore-sieving effect was observed for water adsorbed in (6:6) SWCNs, e.g., the pressure at which the (6:6) SWCNs fill is larger than that at which (8:8) SWCNs fill, in analogy with the results for water adsorption isotherms simulated in carbon-slit pores,[43] and in qualitative agreement with the
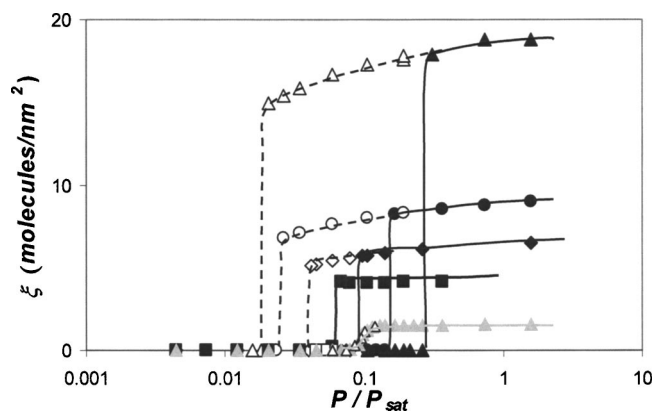

FIG. 2. Simulated adsorption isotherms computed at 298 K. The coverage of the porous surface, ξ (number of adsorbed water molecules per square nanometer of porous surface) is reported as a function of the bulk relative pressure. Triangles are for water adsorption isotherm in (20:20) SWCNs; circles are for water in (12:12) SWCNs; diamonds are for water in (10:10) SWCNs; squares are for water in (8:8) SWCNs; gray triangles are for water in (6:6) SWCNs. Solid symbols are for simulation results along the adsorption path of the isotherm and open symbols are for desorption. Lines are guides for the eye, symbols are larger than statistical uncertainty.

simulation results reported by Noon *et al.*[39] who showed that water molecules cannot be accommodated within (5:5) SWCNs.

In Fig. 3 we report the isosteric heat of adsorption at low coverage, q_{st}, for water adsorbed in (6:6), (8:8), (10:10), (12:12), and (20:20) SWCNs. Values for q_{st} obtained after pore filling (not shown for brevity) exceed the value expected from the enthalpy of liquefaction for SPC/E water [48.8 kJ/mol (Ref. 62)] because the SWCNs considered here are very narrow, as observed previously for both narrow carbon-slit pores[43] and SWCNs.[44] The limit at zero coverage for q_{st} increases as pore diameter decreases. Considering that large positive values for q_{st} indicate strong pore-water attractions, our results indicate that when the pore diameter decreases pore-water interactions become more attractive.

To assess the validity of this physical interpretation of our simulation results, in Fig. 4 we plot the energy profiles for a single water molecule adsorbed within (6:6), (8:8), (10:10), (12:12), and (20:20) SWCNs as a function of the
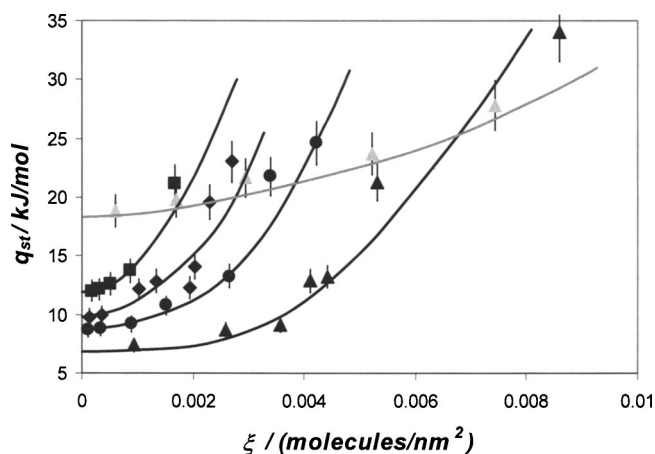

FIG. 3. Isosteric heat of adsorption q_{st} at low coverage for water adsorbed in SWCNs at 298 K. Symbols have the same meaning as in Fig. 2. Lines are guides for the eye.

234712-6   Striolo *et al.*
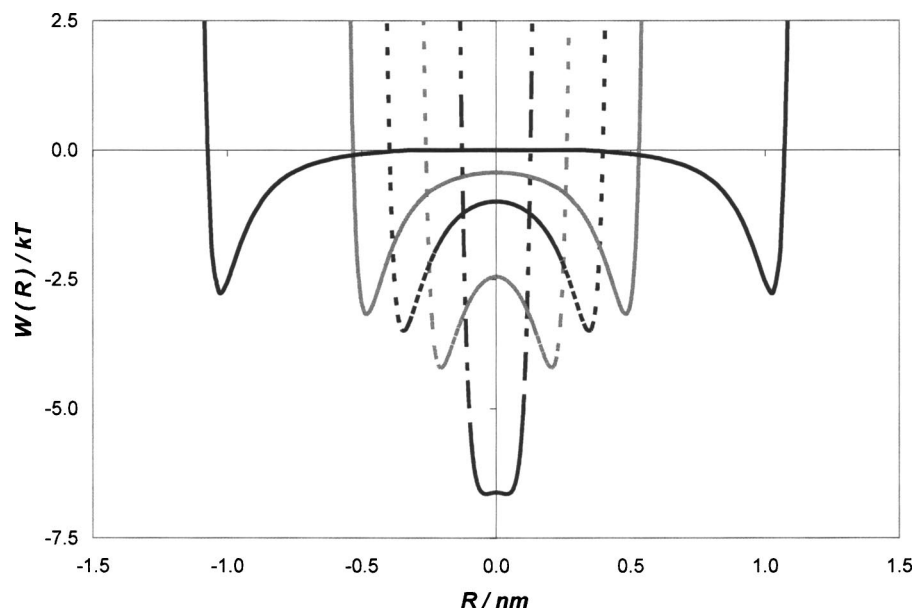
J. Chem. Phys. **122**, 234712 (2005)

FIG. 4. Energy profiles for a water molecule within a (6:6) (black dot-dash line), (8:8) (gray dotted line), (10:10) (black dotted line), (12:12) (gray continuous line), and (20:20) (black continuous line) SWCNs. The pore-water potentials are computed at 298 K.

radial position. These profiles represent the averages obtained for several different positions along the pore axis. Pore-water potentials shown in Fig. 4, combined with the results for q_{st} shown in Fig. 3, indicate that a water molecule is more strongly attracted within narrow cylindrical pores than within larger ones. However, as the diameter increases the degree of confinement increases and water molecules adsorbed within (6:6) SWCNs assume an effective one-dimensional structure. Because of the high degree of confinement, water-water interactions contribute less to q_{st} compared to the situation where water is adsorbed within cylindrical pores of larger diameter. For this reason q_{st} increases more slowly as surface coverage increases when water is adsorbed within (6:6) SWCNs compared to when it is adsorbed within (8:8) or larger SWCNs.

B. Structure of confined water

To better appreciate the effect of confinement upon the structure of confined water, in Fig. 5 we report results for the oxygen- and hydrogen-atom radial density profiles for water confined in (8:8), (10:10), (12:12), and (20:20) SWCNs before and after pore filling at 298 K. In agreement with other reports,[20,35,39] we find that the structure of confined water strongly depends on the diameter of the confining SWCNs. Before pore filling our results suggest that water molecules preferentially adsorb in proximity of the pore wall. However, the amount of water adsorbed at these conditions is not sufficient to form adsorbed monolayers. When the pores are very narrow [see the results for water in (8:8) SWCNs, Fig. 5(a)] water molecules are virtually adsorbed in all the positions available within the tube even before pore filling. The hydrogen-atom radial density profiles obtained for water adsorbed in SWCNs before pore filling differ from those obtained for water adsorbed in carbon-slit pores (see Fig. 9 in Ref. 43). The results shown here [Figs. 5(a), 5(c), 5(e), and 5(f)] suggest that the hydrogen atoms of the first adsorbed water molecules, especially in the narrower pores, face the interior of the pore, thus facilitating hydrogen bonds with

subsequently adsorbed water molecules. This qualitative observation may explain the mechanism behind the faster increase of the isosteric heat of adsorption in (8:8) and wider SWCNs as coverage increases compared to that for water confined in carbon-slit pores (see also Ref. 44).

As noted previously,[28,32,43,44] as soon as a cluster of water molecules forms that spans the whole pore diameter, the pores suddenly and completely fill. After the pores fill, the structure of confined water at 298 K strongly depends on the diameter of the hydrophobic nanopores. When water is confined in (6:6) SWCNs (results not shown for brevity) a one-dimensional chain of hydrogen-bonded molecules is obtained. When water is adsorbed in (8:8) SWCNs [Fig. 5(b)] we observe the formation of one adsorbed monolayer. The hydrogen-atom radial density profile indicates that hydrogen-bonded interactions stabilize this layered structure. When water is confined in (10:10) SWCNs [Fig. 5(d)] we observe the formation of one adsorbed monolayer in contact with the carbon surface and a chain of water molecules confined within the first adsorbed water monolayer. When water is confined in (12:12) SWCNs [Fig. 5(f)] our results predict the formation of two monolayers possibly stabilized by hydrogen bonds as suggested by the elevated hydrogen-atom density in the region between the monolayers. When water is confined in (20:20) SWCNs [Fig. 5(h)] there is the formation of two adsorbed monolayers while water confined deeper within the tube does not show pronounced layered structure.

To visualize the results just discussed, representative snapshots for water confined in (6:6), (8:8), (10:10), and (12:12) SWCNs at 298 K after pore filling are reported in Fig. 6. A visual inspection of the snapshots suggests that water maintains fluidlike properties when confined in (10:10), (12:12), or (20:20) SWCNs [results for water confined in (20:20) SWCNs are not shown here for brevity, but can be found in Ref. 44] while a significant ordering is observed when water is confined within (8:8) SWCNs. The structure obtained for water confined within (8:8) SWCNs appears more ordered compared to that found by Mashl *et al.*[20] We conjecture that a likely source for the mentioned

Downloaded 01 Aug 2005 to 128.219.198.32. Redistribution subject to AIP license or copyright, see http://jcp.aip.org/jcp/copyright.jsp
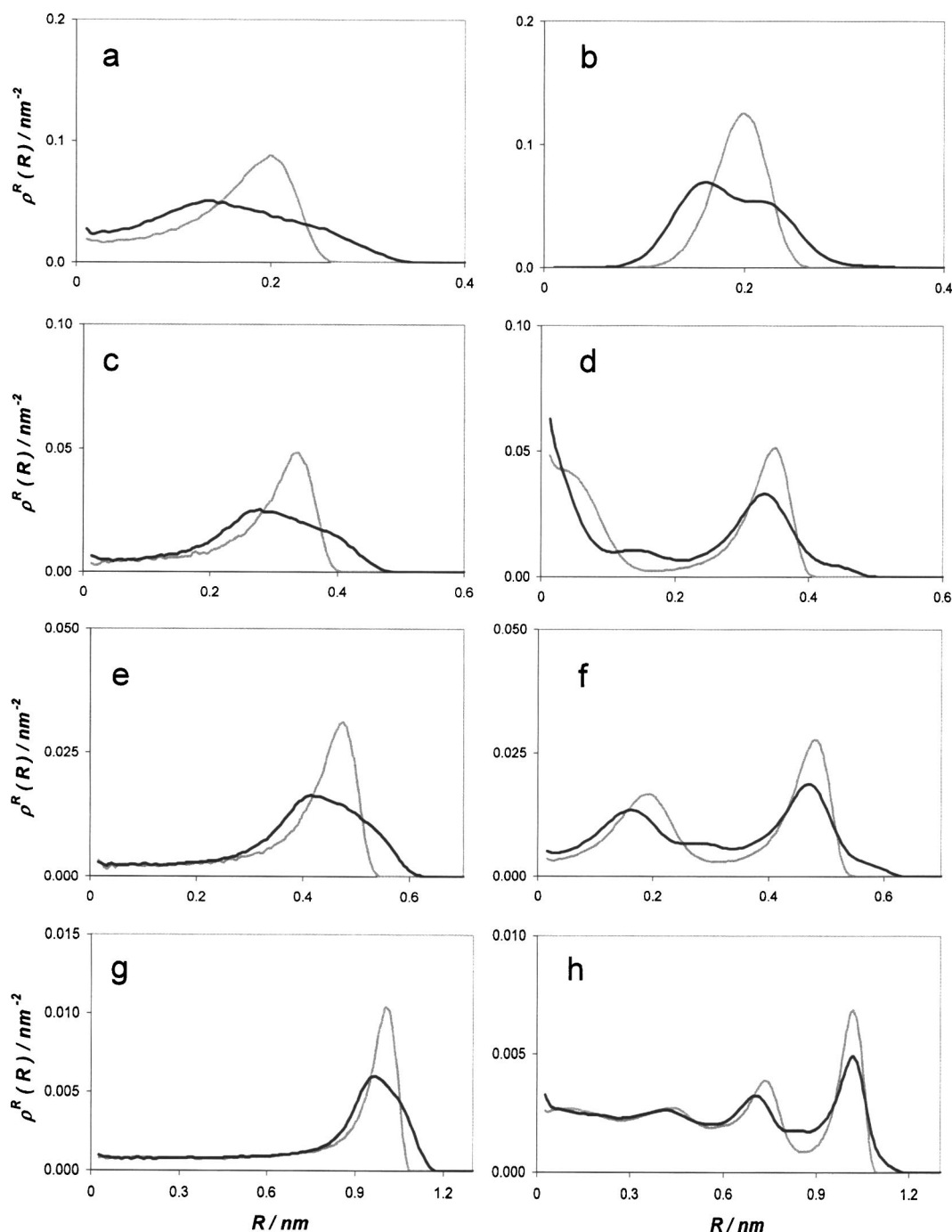
FIG. 5. Oxygen and hydrogen density profiles for water confined in (8:8) [(a) and (b)], (10:10) [(c) and (d)], (12:12) [(e) and (f)], and (20:20) [(g) and (h)] SWCNs. Results are shown before (left-hand figures) and after (right-hand figures) pore filling at 298 K. Gray lines are for oxygen-atom density profiles and black lines are for hydrogen-atom density profiles.

structural difference could be associated with the fact that our SWCNs are effectively infinitely long while those simulated by Mashl *et al.* are only 4.0 nm long and immersed in liquid water at 300 K. The snapshots obtained for water confined in (6:6) SWCNs show that confined water at 298 K after pore filling forms a one-dimensional hydrogen-bonded structure in which each molecule donates one hydrogen atom to form a hydrogen bond with the following molecule and receives one hydrogen atom from the preceding molecule along the tube.

Results for the dipole-dipole correlation function for wa-

ter confined in (6:6) SWCNs at 298 K (see Fig. 10) support the description just discussed. The second hydrogen atom of each adsorbed water molecule does not participate in hydrogen bonds with other adsorbed molecules, but it is instead directed towards the hydrophobic wall. This configuration reproduces the features observed by Mashl *et al.*[20] and those computed by Hummer *et al.*[21] as well as by Mann and Halls[63] for Transferable Intermolecular Potential 3 Points (TIP3P) water model both by classical and by *ab initio* molecular dynamics simulations, and may be representative of the water wires known to exist in naturally occurring biologi-
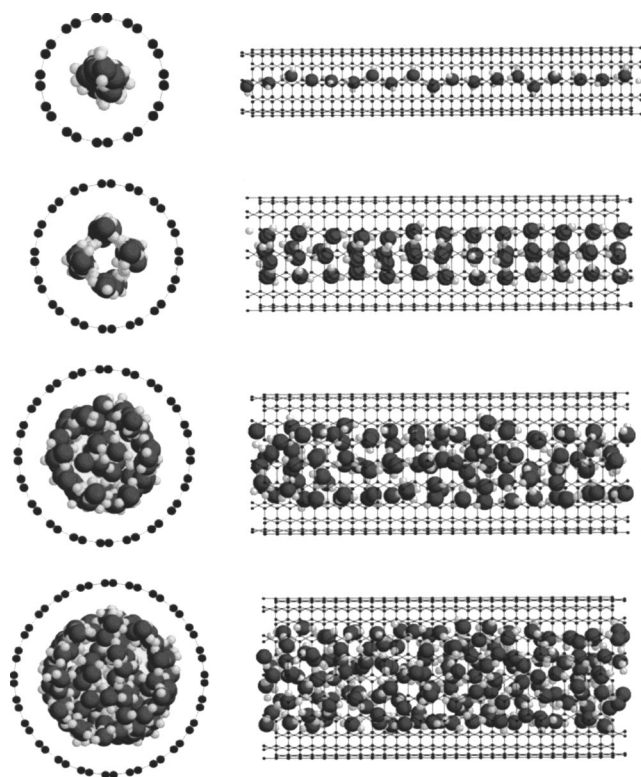
FIG. 6. Front and lateral views of representative simulation snapshots for water adsorbed in SWCNs at 298 K. From top to bottom figures are for water confined in (6:6), (8:8), (10:10), and (12:12) SWCNs. Dark gray spheres represent oxygen atoms and light gray spheres represent hydrogen atoms. Representative snapshots for water confined in (20:20) SWCNs can be found in Ref. 44.

FIG. 7. Order parameters S (a) and T (b) along the pore radii for water confined in (6:6), (8:8), (10:10), (12:12), and (20:20) SWCNs at 298 K.

cal systems (see, for example, Refs. 64 and 65). This structure implies that the number of hydrogen bonds per water molecule is significantly less than the number of hydrogen bonds that a water molecule can establish in bulk liquid or when it is confined in larger pores. This behavior results in an effective loss of energy upon adsorption that is manifested in the pore-sieving effect discussed in Fig. 2, and in the slower increase of q_{st} as surface coverage increases discussed in Fig. 3, even though results for the limit q_{st} at zero coverage (Fig. 3) indicate that a single water molecule is strongly attracted within a (6:6) SWCNs (see also Fig. 4).

The radial dependence of the order parameters S and T are shown in Fig. 7 for water confined in (6:6), (8:8), (10:10), (12:12), and (20:20) SWCNs after pore filling at 298 K. Results for water in (20:20) SWCNs indicate that there is minimal ordering of confined water, except for water in the first two adsorbed monolayers. Our results suggest that the molecules in contact with the carbon surface have a tendency to orient their dipole moments parallel to the pore walls, and then the water molecules in contact with the first adsorbed monolayer tend to orient their dipole moment perpendicular to the pore walls. This relative orientation of the water molecules presumably maximizes the number of hydrogen bonds. The tendency of confined water to form layered ordered structures is accentuated for the case of (12:12) SWCNs because the degree of confinement is larger, and thus confined molecules show a larger propensity for a structurally ordered organization compared to results obtained in
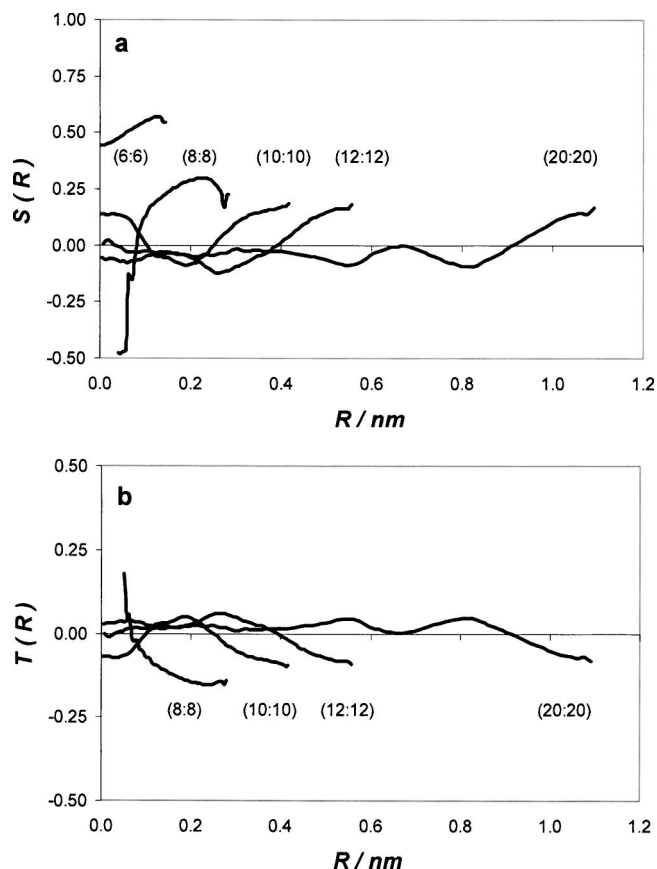
larger pores. When water is confined in (10:10) SWCNs, water molecules belonging to either the first adsorbed monolayer or to the center of the nanopore tend to orient their dipole moments parallel to the pore walls, while those water molecules belonging to the region in between the first adsorbed monolayer and the center of the nanopore tend to orient their dipole moment perpendicular to the pore walls. When water molecules are confined within (8:8) or (6:6) SWCNs, they orient their dipole moments almost parallel to the pore walls, so that they can form chains of hydrogen-bonded molecules, as pictured in Fig. 6.

C. Order-disorder phase transitions

To assess the effect of lowering the temperature on the properties of confined water (we were particularly interested in eventual disorder-to-order phase transitions), we computed additional adsorption isotherms for water in (8:8), (10:10), and (12:12) SWCNs in the temperature range 248–273 K. Results for the adsorption isotherms are not reported here for brevity, since they present features similar to the adsorption isotherms presented in Fig. 2. However, we report the corresponding structural results of confined water at temperatures below room temperature. Oxygen- and hydrogen-atom radial density profiles and oxygen-atom axial density profiles are displayed in Fig. 8 for water confined in (8:8) SWCNs at 273 K and for water confined in (10:10) and in (12:12) SWCNs at 248 K. The results reported refer to the structure of water after pore filling. Although we did not
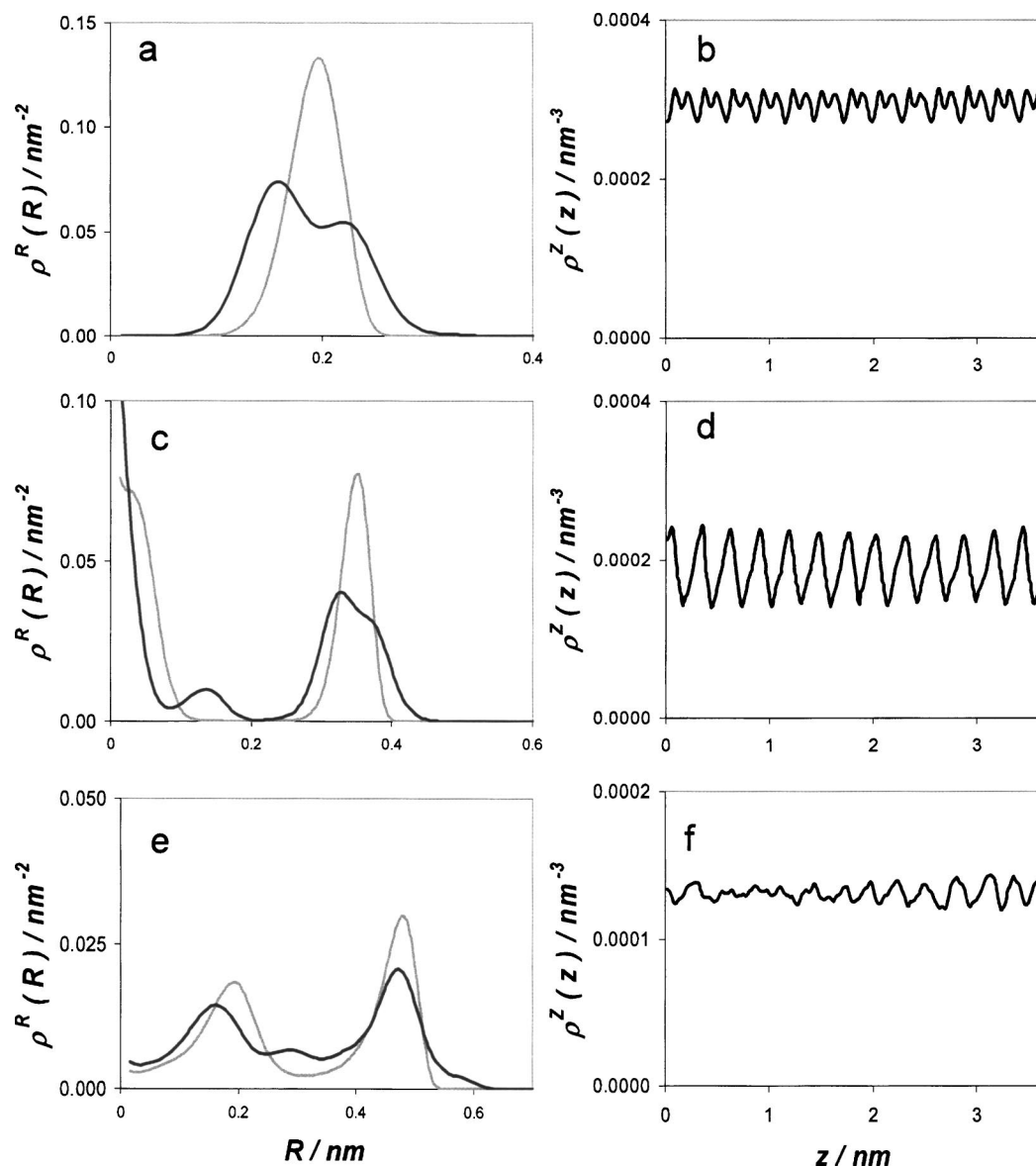
FIG. 8. Atomic density profiles across the pore diameter and along the pore axis for water confined in (8:8) SWCNs at 273 K [(a) and (b)], (10:10) SWCNs at 248 K [(c) and (d)], and (12:12) SWCNs at 248 K [(e) and (f)]. Results are shown after pore filling. Gray lines are for oxygen-atom density profiles and black lines are for hydrogen-atom density profiles.

estimate the pressure at which these structures were obtained, the number of confined water molecules did not change appreciably if compared with those for water adsorbed in SWCNs after pore filling (Figs. 5 and 6); thus the results shown here correspond to an experiment in which carbon pores are first filled with liquid water at ambient conditions, and then cooled to lower temperatures. Results obtained for water in (8:8) SWCNs at this temperature are similar to those obtained at 298 K (see Fig. 5); in addition the oxygen-atom axial density profile [Fig. 8(b)] indicates a significant ordering along the pore axis. To obtain an ordered structure for water confined in (10:10) SWCNs it was necessary to lower the temperature to 248 K [Figs. 8(c) and 8(d)]. The radial density profiles indicate that at these conditions the first adsorbed monolayer is separated from the chain of water molecules in the inner chain (the oxygen-atom radial density profile equals zero in the region between the first adsorbed monolayer and the interior chain). Results obtained

for water confined within (12:12) SWCNs at 248 K [Figs. 8(e) and 8(f)] suggest that a disorder-to-order phase transition has not occurred yet. These observations are summarized in Fig. 9 where representative snapshots are shown for water confined in (8:8) SWCNs at 273 K, and for water confined in (10:10) and (12:12) SWCNs at 248 K. An ordered cubic water nanotube was obtained within (8:8) SWCNs, while an octagonal water nanotube containing a chain of hydrogen-bonded water molecules was obtained in (10:10) SWCNs. Visual analysis of the configuration obtained for water confined in (12:12) SWCNs does not suggest long-ranged ordering even when the temperature is lowered to 248 K.

The cubic and octagonal quasi-one-dimensional water nanotubes that are shown in Fig. 9 are similar to the theoretical predictions by Koga et al.[35,66] for the cubic and the octagonal ice and to the octagonal ice hypothesized by Maniwa et al.[34] for water confined within (10:10) SWCNs at 235 K.
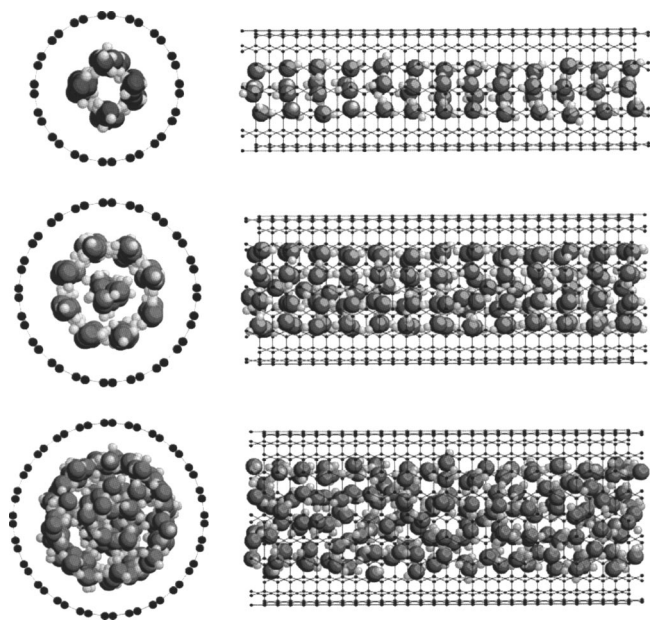
FIG. 9. Front and lateral views of representative simulation snapshots for water adsorbed in SWCNs. From top to bottom figures are for water confined in (8:8) at 273 K, (10:10) at 248 K, and (12:12) SWCNs at 248 K. Dark gray spheres represent oxygen atoms and light gray spheres represent hydrogen atoms.

The nearest-neighbor distances in all structures obtained here are comprised between 0.27 and 0.28 nm, in agreement with results of Koga *et al.*[35] The cubic water nanotube observed within (8:8) SWCNs shows the structural organization described by Koga *et al.*, even though the peak in the oxygen atom density profile across the pore diameter is located at ≈0.2 nm from the center (see Figs. 5 and 8), whereas that found by Koga *et al.* for water in hydrophobic nanotubes of diameter 1.1 nm is located at ≈0.3 nm from the center at 320 K and at ≈0.28 nm at 240 K.[35] These discrepancies are probably due to small differences in the pore-water interaction potentials (the hydrophobic nanotubes used by Koga *et al.* are cylindrical cavities without the atomistic details employed in this work). Other small differences, apparent from visual comparison between the simulation snapshots reported here and those reported in Refs. 35 and 66 are due to thermal

fluctuations, absent in the results reported by Koga *et al.* because those snapshots correspond to the lowest-energy structures. However, our results for water confined in (10:10) SWCNs at 248 K indicate that in addition to the octagonal water nanotube formed in contact with the carbon surface, a chain of hydrogen-bonded water molecules is confined within the unit cell of the octagonal water nanotube. A structure similar to that predicted by Koga *et al.*[66] was found only during desorption of water from a previously filled (10:10) SWCNs at 248 K (results not shown here for brevity). The structure predicted by our GCMC simulations for water confined in (10:10) SWCNs at low temperatures agrees with recent neutron scattering experiments and molecular dynamics calculations by Kolesnikov *et al.*[67]

To characterize further the structural properties of confined water, we computed the dipole-dipole correlation functions for water confined within (6:6), (8:8), and (10:10) SWCNs at 298 K and for water confined within (8:8) and (10:10) SWCNs at 248 K. The resulting dipole-dipole correlation functions are shown in Fig. 10 and indicate a long-range correlation between the dipole moments of water molecules confined within (6:6) SWCNs at 298 K. At this temperature, an increase of the pore diameter decreases the range of dipole-dipole correlation. The dipole moment of water confined within (8:8) SWCNs shows a slowly decaying correlation, while that for confined water within (10:10) SWCNs is limited to the next neighbors. When the temperature is reduced to 248 K water molecules confined in (8:8) SWCNs show a longer range dipole-dipole correlation function than that for 298 K, suggesting a higher degree of ordering for the confined water molecules, as suggested by the snapshots shown in Fig. 9 and by the density profiles shown in Fig. 8. Results for the dipole-dipole correlation function obtained for water confined in (10:10) SWCNs at the two temperatures considered do not differ appreciably from each other.

To allow the molecular-based interpretation of available experimental results, we simulated the x-ray diffraction pattern for water confined in (12:12), (10:10), and (8:8) SWCNs at 298, 273, and 248 K [for water confined within (8:8) SWCNs x-ray diffraction patterns were simulated at 348,
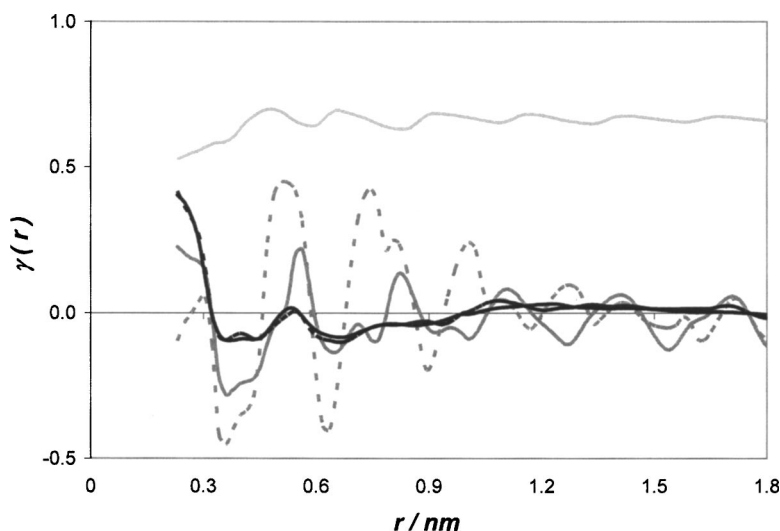

FIG. 10. Dipole-dipole correlation function for water confined in (6:6) (light gray), (8:8) (gray), and (10:10) (black) SWCNs. Results were obtained after pore filling at 298 K (continuous lines) and at 248 K (dotted lines).
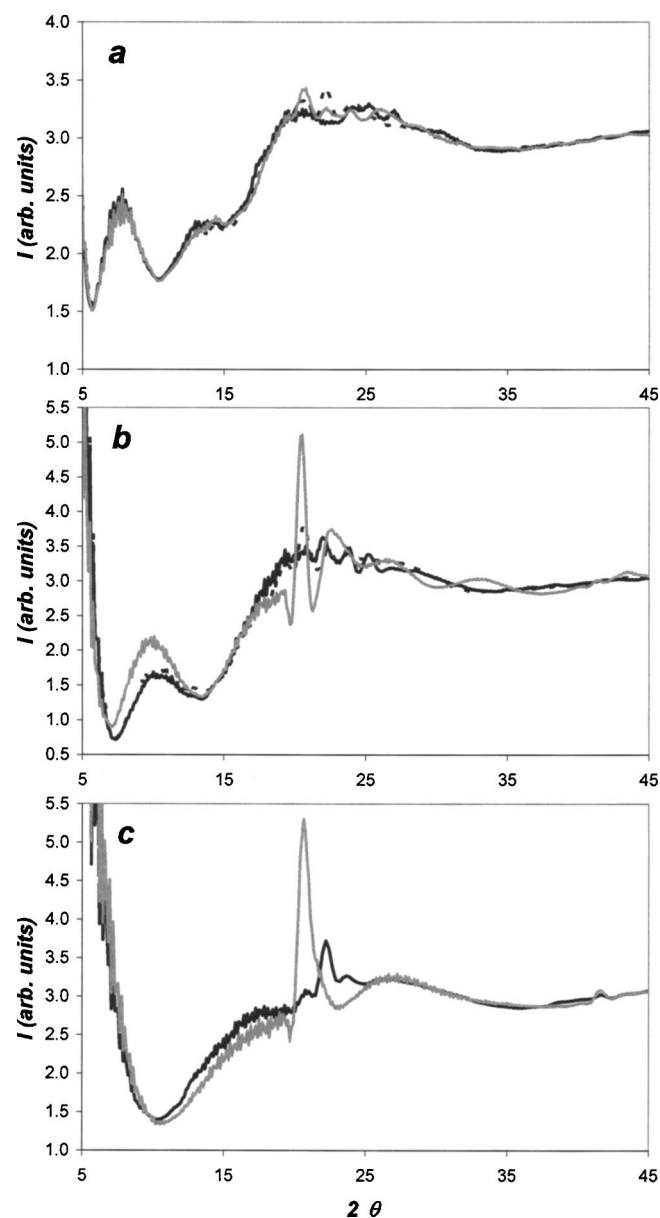
FIG. 11. Simulated diffractograms for water confined in (12:12) (a), (10:10) (b), and (8:8) (c) SWCNs at different temperatures. Black solid, black dotted, and gray solid lines in (a) and (b) are for results obtained at 298, 273, and 248 K, respectively. Black solid line and gray solid line in (c) are for results obtained at 348 and 273 K, respectively. Results at 273 and at 298 K are indistinguishable in (c).
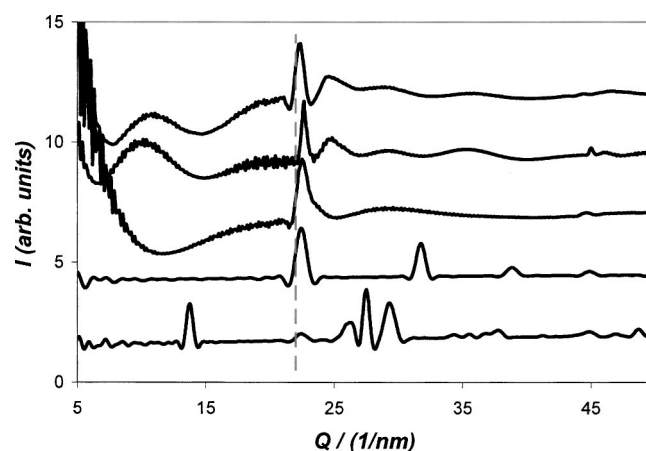

FIG. 12. Comparison between simulated x-ray diffraction patterns. The diffractograms are translated along the y axis to facilitate reading. From top to bottom, the lines represent results for water confined in (10:10) SWCNs at 248 K (see Fig. 11); simulated Debye-functional analysis of a perfect octagonal nanotube; water confined in (8:8) SWCNs at 273 K (see Fig. 11); simulated Debye-functional analysis for a perfect cubic lattice; and simulated Debye-functional analysis for a perfect closed-packed hexagonal lattice. The vertical gray dashed line represents the location of the peak observed by Maniwa *et al.* (Ref. 34) for water confined within (10:10) SWCNs at temperatures below 235 K.

298, and 273 K]. The simulated patterns are shown in Fig. 11. When water is confined within (12:12) SWCNs [Fig. 11(a)] the x-ray diffraction patterns obtained at different temperatures suggest some ordering upon cooling (see peaks at $2\theta = 22°$) especially when the temperature is below 273 K. However, intense peaks representative of crystalline ordering do not appear in the diffraction results. When water is confined within (10:10) SWCNs [Fig. 11(b)], some ordering is observed when the temperature is reduced from 298 to 273 K (see small peaks at about $2\theta = 13°$, peak shifting and appearing in the region from $2\theta = 20°$ to $2\theta = 27°$), but the structure is not formed until the temperature is reduced to 248 K. At these latter conditions a broad peak appears at $2\theta = 10°$ and a narrow but intensive peak grows at $2\theta = 22°$, clearly indicat-

ing the occurrence of a disorder-to-order phase transition. A similar transition occurs when the temperature is reduced from 348 to 298 K for water confined within (8:8) SWCNs [Fig. 11(c)]. In this latter case the x-ray diffraction patterns obtained at 298 and at 273 K are indistinguishable from each other. Due to strong confinement, the structure of water within (8:8) SWCNs differs significantly from those observed in (10:10) and (12:12) SWCNs. For instance, the peaks at $2\theta \cong 7°$ [Fig. 12(a)] or $2\theta \cong 10°$ [Fig. 11(b)] cannot be observed for water confined within (8:8) SWCNs. Recently Morishige and Iwasaki reported experimental x-ray diffraction patterns for water confined in partially filled silica cylindrical pores of radius 3.9 nm.[68] At temperatures below 260 K they observed freezing of the confined water. Their reported diffraction patterns for frozen confined water differ significantly from ours, and suggest the formation of hexagonal ice. This is not unexpected, since the diameter of the pores used by Morishige and Iwasaki is significantly larger than those considered here, and consequently, the structure of confined ice should be similar to that found in bulk ice. To allow comparison between the structures obtained from our GCMC simulations for confined water with those for known crystalline structures, we report in Fig. 12 the simulated x-ray diffraction patterns obtained for a perfect close-packed hexagonal lattice structure, a perfect cubic lattice structure, and a perfect octagonal nanotube, respectively, together with the results just discussed for water confined within (8:8) SWCNs at 273 K and within (10:10) SWCNs at 248 K. The perfect crystal lattices and the perfect nanotube were obtained by imposing a center-to-center distance between next-neighbor oxygen atoms equal to the first peak of the oxygen-oxygen radial distribution function obtained for confined water (0.28 nm, results not shown here for brevity). To facilitate the comparison with the available experimental data, the intensity of the diffracted radiation is plotted in Fig. 12 as
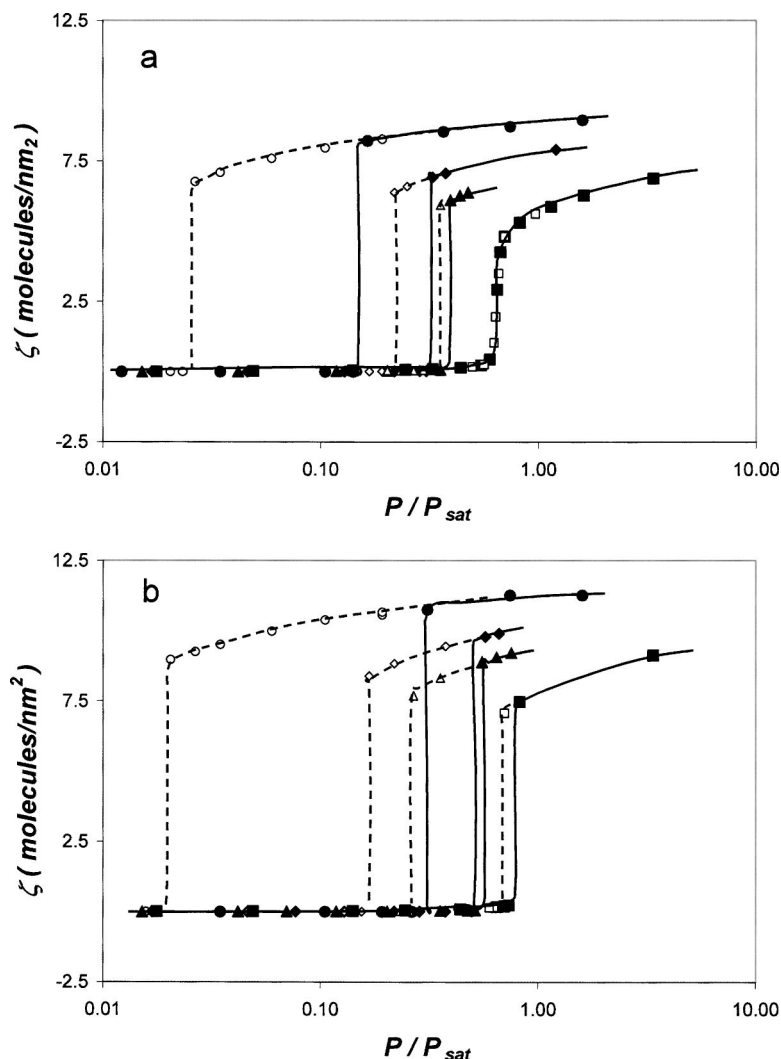
FIG. 13. Simulated water adsorption isotherms in (12:12) (a) and (20:20) (b) SWCNs at different temperatures. Circles are for results obtained at 298 K, diamonds are obtained at 373 K, triangles are obtained at 423 K, and squares are obtained at 498 K. Symbols are larger than computational uncertainty and lines are guides to the eye.

a function of the amplitude of the scattering vector Q $=4\pi \sin(\theta/\lambda)$. In Fig. 12 we also report the location of the peak observed by Maniwa *et al.*[34] for water confined within (10:10) SWCNs and attributed to the formation of ice nanotubes at temperatures below 235 K.

A visual inspection of the results suggests that none of the ordered structures we found for confined water resembles the close-packed hexagonal lattice crystal, while the structure of water confined in (8:8) SWCNs at 248 K is clearly a cubic water nanotube and that of water confined in (10:10) SWCNs at 248 K is an octagonal water nanotube, as also suggested by experimental results by Maniwa *et al.*[34] Small shifts in the peak positions, that indicate different sizes for the unit cells and/or different spacing between atoms, are due to hydrogen bonds, responsible for imperfections in the structure of confined water, and to the fact that confined water is a quasi-one-dimensional and not a tridimensional structure.

D. Adsorption isotherms at large temperatures

In Fig. 13 we report representative simulated water-adsorption isotherms in (12:12) and (20:20) SWCNs at 298, 373, 423, and 498 K. Our simulations predict that as the temperature rises the size of the hysteresis loops becomes smaller and the relative pressure at which pores fill becomes

larger. This behavior is in qualitative agreement with both experiment and simulation of simple fluids[69] and water.[26,31,70] By simulating adsorption isotherms at increasing temperatures we obtained the hysteresis critical temperature for water adsorbed in SWCNs. Our simulation results indicate that the hysteresis critical temperature, defined as the lowest temperature at which no hysteresis can be detected, is 543±10, 443±10, and 368±5 K when SPC/E water is adsorbed in (20:20), (12:12), and (10:10) SWCNs, respectively. Experimental results indicate that reversible adsorption isotherms are obtained for water in (10:10) SWCNs at 450 K,[34] in reasonable agreement with our findings. For comparison, the vapor-liquid coexistence curve for bulk SPC/E water is $\approx$635 K.[71]

IV. CONCLUSIONS

Grand canonical Monte Carlo simulations were used to study water adsorption in (6:6), (8:8), (10:10), (12:12), and (20:20) single-walled carbon nanotubes in the temperature range 248–548 K. The 298 K adsorption isotherms exhibit the typical features of the type V adsorption isotherms in the IUPAC classification, the water uptake is negligible at low pressures; pores suddenly and completely fill once a threshold pressure is reached; the adsorption-desorption loops are

characterized by wide hysteresis. The width of the hysteresis loops decreases as pore diameter narrows. Adsorption isotherms simulated in (6:6) and (8:8) SWCNs at 298 K do not show adsorption-desorption hysteresis loops, and the water uptake in (6:6) SWCNs is gradual as the pressure increases. For water adsorbed within (20:20), (12:12), (10:10), and (8:8) SWCNs the relative pressure at which pores fill at 298 K decreases as the pore diameter decreases. Adsorption isotherms simulated in (6:6) SWCNs at 298 K show a pore-sieving effect [(6:6) SWCNs fill at pressures larger than those at which (8:8) SWCNs do].

The structure of confined water depends on the diameter of the SWCNs. Radial density profiles obtained at 298 K indicate a pronounced layered structure when water is confined within (12:12), (10:10), and (8:8) SWCNs. Water confined in (6:6) SWCNs at 298 K forms one-dimensional hydrogen-bonded chains in which each water molecule receives one hydrogen from the preceding molecule and donates one hydrogen to the following molecule along the chain. A high degree of confinement for water adsorbed within (8:8) and (10:10) SWCNs induces a disorder-to-order phase transition to cubic [water in (8:8) SWCNs] or octagonal (water in (10:10) SWCNs) water nanotubes at 298 and 248 K, respectively. The x-ray diffraction patterns support our findings.

Our results for water adsorption isotherms in (10:10), (12:12), and (20:20) SWCNs in the 298–548 K temperature range indicate that the width of the hysteresis loop decreases as temperature rises, and that the relative pressure at which pores fill increases as temperature increases. The hysteresis critical temperature is found to be 543 ± 10, 443 ± 10, and 368 ± 5 K for water adsorbed in (20:20), (12:12), and (10:10) SWCNs, respectively.

ACKNOWLEDGMENTS

[1] S. Iijima, Nature (London) **354**, 56 (1991).
[2] T. W. Ebbesen, in Carbon Nanotubes, Preparation and Properties, *Production and Purification of Carbon Nanotubes*, edited by T. W. Ebbesen (CRC Boca Raton, FL, 2000).
[3] P. M. Ajayan and T. W. Ebbesen, Rep. Prog. Phys. **60**, 1025 (1997).
[4] S. Iijima and T. Ichibashi, Nature (London) **363**, 603 (1993).
[5] D. S. Bethune, C. H. Kiang, M. S. de Vries, G. Gorman, R. Savoy, J. Vazquez, and R. Beyers, Nature (London) **363**, 605 (1993).
[6] J. W. Mintmire, B. I. Dunlap, and C. T. White, Phys. Rev. Lett. **68**, 631 (1992).
[7] N. Hamada, S.-i. Sawada, and A. Oshiyama, Phys. Rev. Lett. **68**, 1579 (1992).
[8] K. Tanaka, K. Okanhara, N. Okada, and T. Yamabe, Chem. Phys. Lett. **191**, 469 (1992).
[9] A. Lueking and R. T. Yang, AIChE J. **49**, 1556 (2003).
[10] M. D. Halls and H. B. Schlegel, J. Phys. Chem. B **106**, 1921 (2002).
[11] J. Zhao, A. Buldum, J. Han, and J. P. Lu, Nanotechnology **13**, 195 (2002).
[12] J. Kong, N. R. Franklin, C. Zhou, M. G. Chapline, S. Peng, K. Cho, and H. Dai, Science **287**, 622 (2000).
[13] P. G. Collins, K. Bradley, M. Ishigami, and A. Zettl, Science **287**, 1801 (2000).
[14] C.-H. Kiang, J.-S. Choi, T. T. Tran, and A. D. Bacher, J. Phys. Chem. B **103**, 7449 (1999).
[15] M. Monthioux, Carbon **40**, 1809 (2002).
[16] A. Kalra, S. Garde, and G. Hummer, Proc. Natl. Acad. Sci. U.S.A. **100**, 10175 (2003).
[17] M. Wilson, Chem. Phys. Lett. **366**, 504 (2002).
[18] D. Nicholson and K. E. Gubbins, J. Chem. Phys. **104**, 8126 (1996).
[19] M. S. P. Sansom and P. C. Biggin, Nature (London) **414**, 156 (2001).
[20] R. J. Mashl, S. Joseph, N. R. Aluru, and E. Jacobsson, Nano Lett. **3**, 589 (2003).
[21] G. Hummer, J. C. Rasaiah, and J. P. Noworyta, Nature (London) **414**, 188 (2001).
[22] A. Waghe, J. C. Rasaiah, and G. Hummer, J. Chem. Phys. **117**, 10789 (2002).
[23] F. Rouquerol, J. Rouquerol, and K. Sing, *Adsorption by Powders and Porous Solids* (Academic, London, 1999).
[24] E. A. Müller, L. F. Rull, L. F. Vega, and K. E. Gubbins, J. Phys. Chem. **100**, 1189 (1996).
[25] C. L. McCallum, T. J. Bandosz, S. C. McGrother, E. A. Müller, and K. E. Gubbins, Langmuir **15**, 533 (1999).
[26] J. K. Brennan, T. Bandosz, K. T. Thomson, and K. E. Gubbins, Colloids Surf., A **187-188**, 539 (2001).
[27] J. K. Brennan, K. T. Thomson, and K. E. Gubbins, Langmuir **18**, 5438 (2002).
[28] M. Jorge and N. A. Seaton, AIChE J. **49**, 2059 (2003).
[29] A. M. Slasli, M. Jorge, F. Stoekli, and N. A. Seaton, Carbon **41**, 479 (2003).
[30] E. N. Rudisill, J. J. Hacskaylo, and M. D. LaVan, Ind. Eng. Chem. Res. **31**, 1122 (1992).
[31] S. J. Gregg and K. S. W. Sing, *Adsorption, Surface Area and Porosity* (Academic, London, 1982).
[32] M. Jorge, C. Schumacher, and N. A. Seaton, Langmuir **18**, 9296 (2002).
[33] E. Bekyarova, Y. Hanzawa, K. Kaneko et al. Chem. Phys. Lett. **366**, 463 (2002).
[34] Y. Maniwa, H. Kataura, M. Abe, S. Suzuki, Y. Achida, H. Kira, and K. Matsuda, J. Phys. Soc. Jpn. **71**, 2863 (2002).
[35] K. Koga, G. T. Gao, H. Tanaka, and X. C. Zeng, Nature (London) **412**, 802 (2001).
[36] J. Martí and M. C. Gordillo, Phys. Rev. B **63**, 165430 (2001).
[37] J. Martí and M. C. Gordillo, Chem. Phys. Lett. **354**, 227 (2002).
[38] I. Brovchenko, A. Geiger, A. Oleinikova, and D. Paschek, Eur. Phys. J. E **12**, 69 (2003).
[39] W. H. Noon, K. D. Ausman, R. E. Smalley, and J. Na, Chem. Phys. Lett. **355**, 445 (2002).
[40] I. Brovchenko, A. Geiger, and A. Oleinikova, Phys. Chem. Chem. Phys. **3**, 1567 (2001).
[41] J. L. Rivera, C. McCabe, and P. T. Cummings, Nano Lett. **2**, 1427 (2002).
[42] A. Giaya and R. W. Thompson, J. Chem. Phys. **117**, 3464 (2002).
[43] A. Striolo, A. A. Chialvo, P. T. Cummings, and K. E. Gubbins, Langmuir **19**, 8583 (2003).
[44] A. Striolo, K. E. Gubbins, A. A. Chialvo, and P. T. Cummings, Mol. Phys. **102**, 243 (2004).
[45] M. Jorge and N. A. Seaton, Mol. Phys. **100**, 3803 (2002).
[46] A. Striolo, P. K. Naicker, A. A. Chialvo, P. T. Cummings, and K. E. Gubbins, Adsorption (in press).
[47] A. Striolo, K. E. Gubbins, A. A. Chialvo, and P. T. Cummings, Adsorption (in press).
[48] M. C. Gordillo and J. Martí, Chem. Phys. Lett. **341**, 250 (2001).
[49] H. J. C. Berendsen, J. R. Grigera, and T. P. Straatsma, J. Phys. Chem. **91**, 6269 (1987).
[50] W. A. Steele, *The Interaction of Gases with Solid Surfaces* (Pergamon, Oxford, 1974).
[51] D. Nicholson and N. G. Parsonage, *Computer Simulation and the Statistical Mechanics of Adsorption* (Academic, London, 1982).
[52] M. P. Allen and D. J. Tildesley, *Computer Simulation of Liquids* (Claredon, Oxford, 1987).
[53] D. Frenkel and B. Smit, *Understanding Molecular Simulation*, 2nd ed. (Academic, London, 2002).

[54] J.-C. Liu and P. A. Monson, Langmuir (to be published).

[55] A. Pertsin and M. Grunze, J. Phys. Chem. B **108**, 1357 (2004).

[56] L. Sarkisov and P. A. Monson, Langmuir **16**, 9857 (2002).

[57] E. Kierlik, P. A. Monson, M. L. Rosinberg, L. Sarkisov, and G. Tarjus, Phys. Rev. Lett. **87**, 055701 (2001).

[58] V. Gnutzmann and W. Vogel, J. Phys. Chem. **94**, 4991 (1990).

[59] P. Debye, Ann. Phys. **46**, 809 (1915).

[60] D. A. H. Cunningham, W. Vogel, R. M. Torres Sanchez, K. Tanaka, and M. Haruta, J. Catal. **183**, 24 (1999).

[61] D. T. Cromer and J. B. Mann, Acta Crystallogr., Sect. A: Cryst. Phys., Diffr., Theor. Gen. Crystallogr. **A24**, 321 (1968).

[62] A. Glättli, X. Daura, and W. F. van Gunsteren, J. Chem. Phys. **116**, 9811 (2002).

[63] D. J. Mann and M. D. Halls, Phys. Rev. Lett. **90**, 195503 (2003).

[64] M. H. B. Stowell, T. M. McPhillips, D. C. Rees, S. M. Soltis, E. Abresch, and G. Feher, Science **276**, 812 (1997).

[65] E. Tajikhorshid, P. Nollert, M. Ø. Jensen, L. J. W. Miercke, J. O'Connell, R. M. Stroud, and K. Schulten, Science **296**, 525 (2002).

[66] K. Koga, R. D. Parra, H. Tanaka, and X. C. Zeng, J. Chem. Phys. **113**, 5037 (2000).

[67] A. I. Kolesnikov, J.-M. Zanotti, C.-K. Loong, P. Thiyagarajan, A. P. Moravsky, R. O. Loufty, and C. J. Burnham, Phys. Rev. Lett. **93**, 035503 (2004).

[68] K. Morishige and H. Iwasaki, Langmuir **19**, 2808 (2003).

[69] K. Morishige and N. Tateishi, J. Chem. Phys. **119**, 2301 (2003).

[70] A. Striolo, K. E. Gubbins, M. S. Gruszkiewicz *et al.*, Langmuir (to be published).

[71] T. M. Hayward and I. M. Svishchev, Fluid Phase Equilib. **182**, 65 (2001).